Measurement 251 (2025) 117206

Contents lists available at ScienceDirect

Measurement

journal homepage: www.elsevier.com/locate/measurement

A novel six-dimensional micro-vibration measurement platform calibrated by transfer learning DNN

Haodong Cui [a,b,c], Mingming Xu [a,b,*], Jiangpei Dou [a,b]

[a] Nanjing Institute of Astronomical Optics & Technology, Chinese Academy of Sciences, Nanjing 210042, China
[b] CAS Key Laboratory of Astronomical Optics & Technology, Nanjing Institute of Astronomical Optics & Technology, Nanjing 210042, China
[c] University of Chinese Academy of Sciences, Beijing 100049, China

ARTICLE INFO

Keywords:
Micro-vibration
Vibration testing
Finite element analysis
Dynamic calibration
Transfer learning

ABSTRACT

In this paper, we developed a micro-vibration measurement platform using five piezoelectric sensors. Compared to the traditional four-sensor measurement configuration, this design offers enhanced stiffness and expands the measurable frequency bandwidth. Through finite element analysis and optimized design, we determined the structural parameters of the platform and maximized its fundamental frequency. Additionally, a novel transfer learning algorithm was implemented for dynamic calibration. Within the calibration frequency band, this transfer learning approach utilizes the optimized parameters of the deep neural network (DNN) from the previous frequency as the initialization parameters for the next frequency. This process enables the reuse of structural information across the entire frequency band, thereby improving the network's convergence rate and reducing the workload required for tuning training parameters. The calibrated platform can accurately measure generalized forces within the frequency range of 10 ~ 600 Hz. The relative errors for the three-dimensional forces *Fx*, *Fy* and *Fz* are 2.38 %, 1.39 %, and 2.80 %, respectively, while those for the three-dimensional moments are 2.18 %, 2.65 %, and 1.90 %. These results indicate that the calibrated measurement platform meets the requirements for precise measurements.

1. Introduction

Vibration monitoring based on multi-dimensional component measurement has important applications in various fields such as robotics, precision machining, and aerospace. By measuring the three-axis acceleration or six-dimensional generalized forces (*Fx*, *Fy*, *Fz*, *Mx*, *My*, *Mz*) at specific locations within a motion mechanism, it enables key functions such as control optimization [1,2], vibration suppression [3–5], and structural health monitoring [6,7].

Among the various scenarios that require vibration monitoring, satellite micro-vibration testing and control present new challenges. In recent years, the observation satellites under construction are not only larger and heavier than their predecessors, but their micro-vibration control requirements have also become more stringent. For instance, the China Space Station Telescope (CSST) features a primary mirror with a diameter of 2 m and a total mass of 15 tons [8–10], yet it is designed to maintain on-orbit micro-vibrations of less than 0.4 N. Furthermore, some proposed space telescopes, such as the planned optical satellites in Tianqin [11] and LISA [12], have even more stringent micro-vibration requirements with an absolute pointing accuracy of around 2.1×10^{-3} arcseconds.

Traditionally, the effects of micro-vibration usually could be evaluated through single-source testing or by performing integrated opto-mechanical analyses on the entire satellite. However, in this approach, analyzing the impact of a single vibration source on the overall system structure necessitates the installation of the entire opto-mechanical assembly—a step that is infeasible when subsystems are still in the design phase. Once all subsystems are available for testing, it becomes difficult to make substantial modifications to the micro-vibration isolation system design. To address this challenge, we aim to evaluate micro-vibration effects by treating each vibration source and its associated subsystem as a unified testing unit. This method retains the flexibility and convenience of stand-alone testing while also capturing the impact of individual vibration sources on the overall load-bearing structure, thereby providing a valuable reference for designing effective micro-vibration isolation systems.

Currently, the main challenge in performing micro-vibration testing at the satellite subsystem level is the increasing size of the Device Under

* Corresponding author at: Nanjing Institute of Astronomical Optics & Technology, Chinese Academy of Sciences, Nanjing 210042, China.
E-mail addresses: hdcui@niaot.ac.cn (H. Cui), mingxu@niaot.ac.cn (M. Xu), jpdou@niaot.ac.cn (J. Dou).

https://doi.org/10.1016/j.measurement.2025.117206
Received 17 November 2024; Received in revised form 3 March 2025; Accepted 5 March 2025
Available online 5 March 2025

Test (DUT). For smaller DUTs that are typically less than 250 mm × 250 mm in size, measurements can usually be performed with accelerometers, force transducers, or small force measurement platforms [13–18]. However, for complex modules that incorporate both a vibration source and additional structural components, the projection area can approach 1 m × 1 m, which exceeds the capacity of current force measurement platforms. Consequently, researchers have investigated constructing large-scale micro-vibration measurement platforms to address this limitation.

Previously, most research on large-scale force measurement platforms focuses on the research and application of the Stewart platform [19–23]. However, this design is not suitable for micro-vibration testing. The quilted structure between the upper and lower plates makes its fundamental frequency too low to achieve the requirements of measuring high-frequency dynamic forces. Thus, exploring new configurations for measurement platforms has become necessary.

There are two primary challenges in constructing a large-scale micro-vibration measurement platform. First, as platform size increases, its fundamental frequency decreases rapidly, which restricts the measurement bandwidth range as the operating bandwidth must avoid the fundamental frequency. Researchers have made significant efforts to address this through structural design improvements. For example, Li et al. [24] and Zhou et al. [25–27] enhanced the fundamental frequency of the measurement platform by adding load-sharing structures or using a ring-shaped upper plate. Additionally, Xia et al. [28] maintained high stiffness in larger platforms by optimizing the sensor array arrangement, utilizing 16 sensors. Furthermore, commercial products have demonstrated a trend toward using high-stiffness, lightweight materials for the upper plates. For instance, in two models of Kistler force measurement platforms, replacing stainless steel with ceramic for the upper plate increased the fundamental frequencies in the x, y, and z directions by 18 %, 18 %, and 36 %, respectively, without altering the plate size [29,30].

The second major challenge is the dynamic calibration of the measurement platform. In many previous studies, researchers used generalized inverse matrix for calibration [31,32], which simplifies data acquisition and processing. However, this linear-fitting approach overlooks the platform's inherent nonlinearity, thereby limiting measurement accuracy improvements. Recently, the importance of nonlinear models for calibration has become more widely recognized, and researchers have begun applying neural network models to sensor calibration [33–36]. In the context of platform calibration, Zhou explored two neural network methods for calibration [27,37]. Compared to the traditional generalized inverse matrix method, neural network calibration achieves nonlinear fitting, resulting in improved measurement accuracy. However, none of the neural network calibration methods mentioned above make use of the structural continuity of the sensor or the measurement platform across the frequency domain, which would leading to a lack of connection between neural networks at different frequency points, resulting in inefficiencies and discontinuities in training and parameter tuning.

In this paper, to solve the problem of ground micro-vibration testing for large payloads, we investigated the design, construction, and calibration of a large-scale measurement platform, addressing the two challenges mentioned above. In Section 2, we present the development of our measurement platform using five sensors. Through finite element analysis and parameter optimization, we designed a 500 mm × 500 mm platform while ensuring a high fundamental frequency. In Section 3, we proposed a novel transfer learning DNN for calibrating the measurement platform, which more effectively captures the nonlinear behavior of the platform under excitation. In Section 4, we conduct comprehensive tests on the calibrated measurement platform and calculate the output errors in six dimensions. The results demonstrate the feasibility and accuracy of the entire measurement system. Finally, in Section 5, we summarize the conclusions and discuss the potential of extending this measurement setup to other fields.

2. Structural design

Conventional multi-dimensional generalized force measurement platforms typically use four sensors arranged in a rectangular configuration. This design is simple, facilitates calculations, and reduces costs. However, as the size of the measurement platform increases, this configuration significantly reduces the fundamental frequency. To address this issue, we added an additional sensor at the center to enhance the stiffness of the platform. Fig. 1 illustrates the fundamental frequency of both the conventional four-sensor configuration and our five-sensor configuration as the platform size increases, and the only difference is whether or not a 5th sensor is present in the center. When the upper plate is small, the improvement in the fundamental frequency with the five-sensor configuration is not substantial. However, as the size of the upper plate increases, the advantage of the five-sensor configuration in terms of the fundamental frequency becomes more pronounced.

Fig. 2 illustrates the structure of the measurement platform, with five piezoelectric sensors (Kistler 9367C) mounted between the upper and lower plates. During measurements, the vibration source is attached to the upper plate, while the lower plate is fixed to the foundation. To maximize the fundamental frequency, specific parameters of the plate were optimized during the design process.

2.1. Upper plate design and optimization

The design of the upper plate has a substantial impact on the fundamental frequency of the measurement platform. Consequently, this section focuses on the optimization of the upper plate's design parameters. We utilized the finite element model shown in Fig. 3(a) to conduct the relevant simulations. In this model, the top surfaces of the five sensors are considered bolted and in frictional contact with the upper plate, while the bottom surfaces are fully constrained. To streamline the simulation, the lower plate, which serves as part of the foundation, was omitted to prevent local modes that might distort the simulation results. Furthermore, by excluding the frictional interactions between the lower plate, bolts, and sensors, this simplification reduces the computational resources required.

In our design, the upper plate is constructed from titanium alloy (TC4), with the optimization parameters summarized in Fig. 3(b) and Table 1. During the preliminary analysis, we simulated how four key parameters affect the fundamental frequency. With the maximum fundamental frequency as the optimization objective, we used the Genetic Algorithm (GA) for optimization. The flowchart of the algorithm and the optimization computation process are presented in Fig. 4 and Fig. 5, respectively. Based on the results in Fig. 5, along with additional validation, we observed that variables H and L have a monotonic effect on the fundamental frequency within the specified range. Consequently, their values were set to the minimum permissible within the allowable range: $L = 500$ mm and $H = 40$ mm.

To further explore the effects of variations in the other parameters, we calculated 64 evenly distributed points within the ranges of l and h and generated the contour plot shown in Fig. 6, which indicates that the maximum fundamental frequency occurs around $h = 25$ mm and $l = 322$ mm. After further refinement, considering machining complexity and potential errors, we selected $h = 24.4$ mm and $l = 310$ mm, achieving a fundamental frequency of 1034 Hz. All relevant parameters have been calculated and are summarized in Table 2.

2.2. Structural FEA and testing

In Section 2.1, we determined the parameters of the upper plate; however, additional structural information is needed for further analysis. Therefore, we used the same finite element model shown in Fig. 2 (a) to calculate the first four modes of the structure, with results displayed in Fig. 7. The first and second modes are characterized by

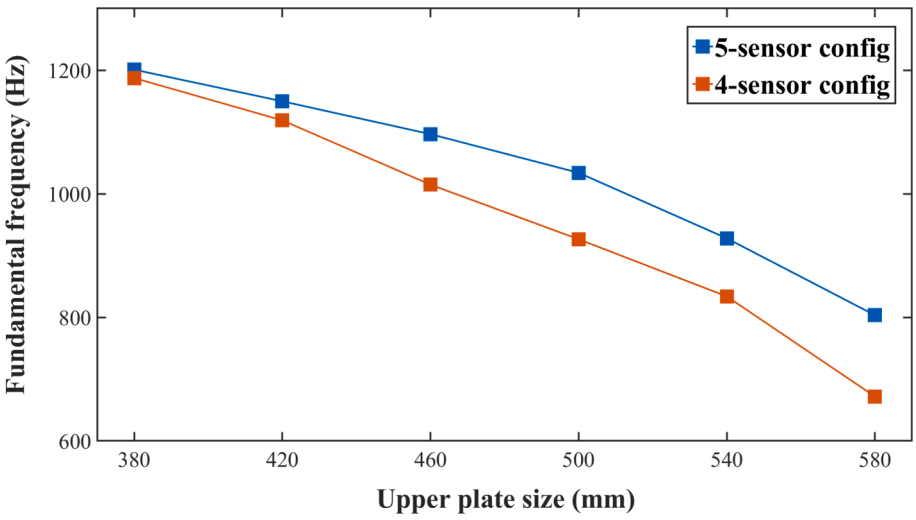

Fig. 1. Comparison of fundamental frequencies between 4-sensor and 5-sensor configurations.

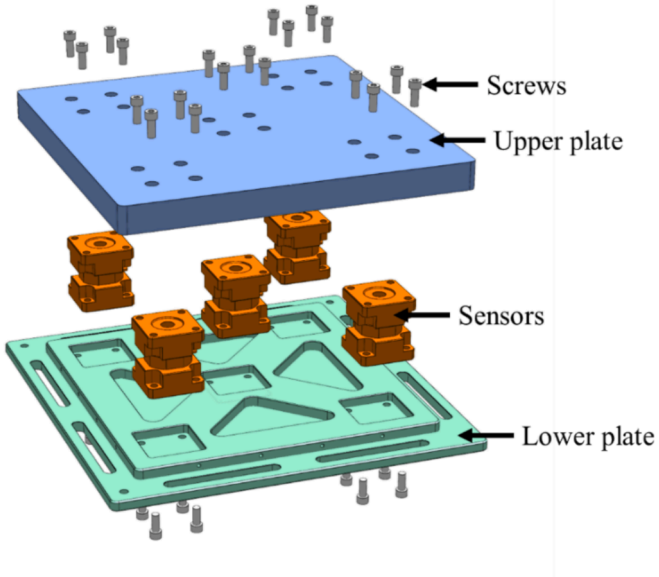

Fig. 2. Measurement platform layout.

extrusion and translation in two different directions along the surface, the third mode is torsional, and the fourth mode is bending.

To facilitate comparison with experimental results, we also analyzed the complete structure, including the lower plate. The first four modal shapes and their corresponding frequencies are shown in Fig. 8. A comparison between Fig. 7 and Fig. 8 reveals that the first- and third-order modes are swapped, which is expected due to their close frequency intervals. Additionally, the inclusion of the lower plate has a negligible impact on the calculated frequencies of the first four modes, supporting the reasonableness of the simplifications made during the optimization of the upper plate parameters.

Based on the previous analysis and design, we fabricated the measurement platform and conducted structural testing. As shown in Fig. 9, we performed a modal test on the platform using 10 accelerometers (LNS 802Y31), with 9 accelerometers arranged evenly on the upper plate to capture vibration data and 1 placed on the mounting base to record the weak coupling of the mounting foundation under excitation from the impact hammer.

Using data from the 9 accelerometers on the upper plate, Fig. 10 presents the modal test results of the platform, confirming the fundamental frequency of 996.09 Hz. This reveals a 3.8 % relative error compared to the 1034 Hz frequency predicted by finite element analysis. Considering potential error sources such as machining and installation inaccuracies, as well as the coupling effect between the platform and the foundation, this error is within an acceptable range. These experimental

Table 1
Optimization parameters and value ranges.

Parameter	Range
L	$\geq$500 mm
l	220 ~ 400 mm
H	40 ~ 50 mm
h	0 ~ 40 mm

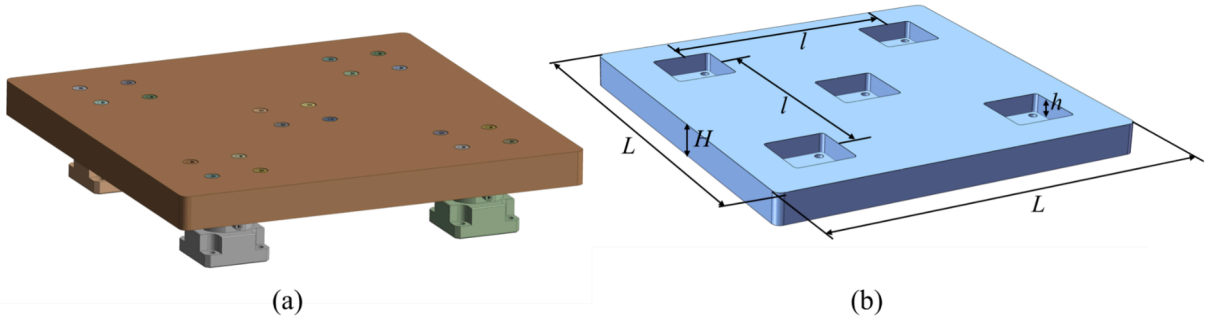

Fig. 3. Upper plate: (a) Finite element model; (b) Parameters to be optimized.

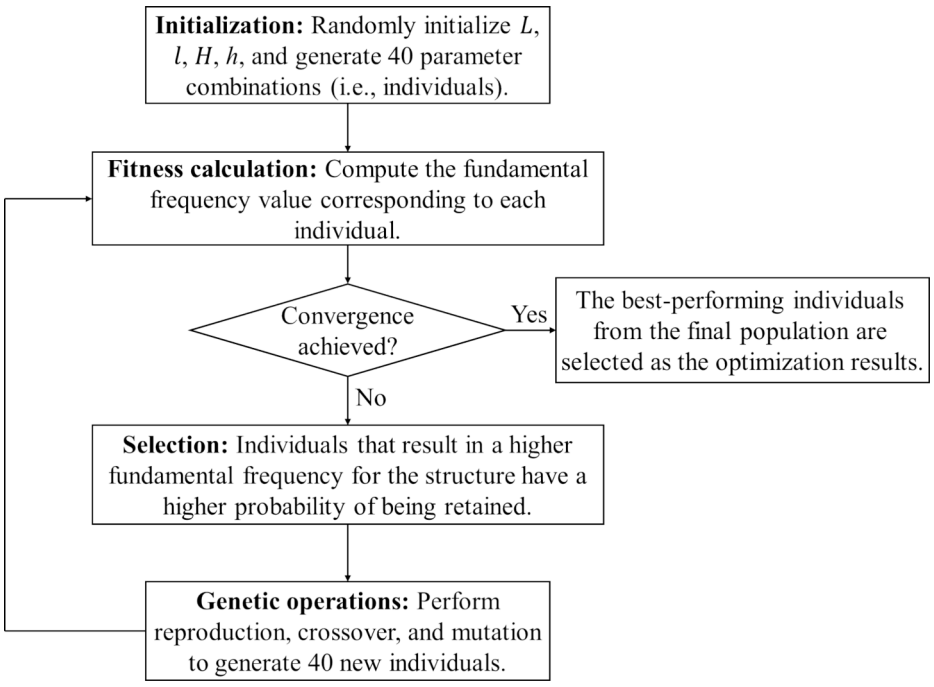

Fig. 4. Flowchart of the GA.

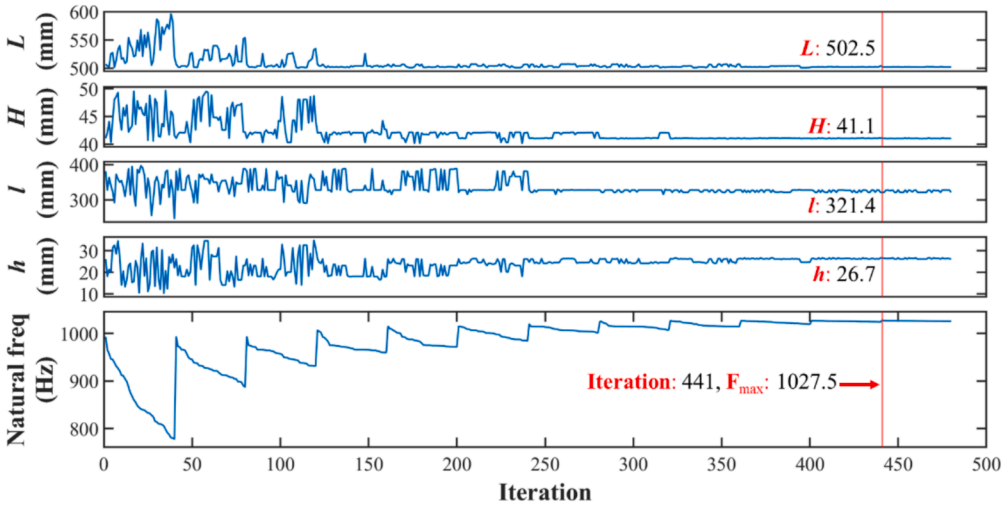

Fig. 5. Optimization process using the GA.

results validate the accuracy of our finite element simulation and underscore its significance in optimizing the platform design, a crucial aspect for the development of measurement platforms.

3. Calibration

When positioned away from the fundamental frequency, the measurement platform can be treated as a rigid body, and the measurement results are obtained from the responses of the five three-component sensors using Eq. (1). In which d_{ni} represents the shortest vector of axis n pointing toward sensor i, while F_{ni} represents the response of sensor i in direction n.

$$\begin{cases} F_x = \sum_{i=1}^{i=5} F_{xi} \\ F_y = \sum_{i=1}^{i=5} F_{yi} \\ F_z = \sum_{i=1}^{i=5} F_{zi} \\ M_x = \sum_{i=1}^{i=5} d_{xi} \times F_{yi} + \sum_{i=1}^{i=5} d_{xi} \times F_{zi} \\ M_y = \sum_{i=1}^{i=5} d_{yi} \times F_{xi} + \sum_{i=1}^{i=5} d_{yi} \times F_{zi} \\ M_z = \sum_{i=1}^{i=5} d_{zi} \times F_{xi} + \sum_{i=1}^{i=5} d_{zi} \times F_{yi} \end{cases} \quad (1)$$

The sensors used in this setup were factory-calibrated, which

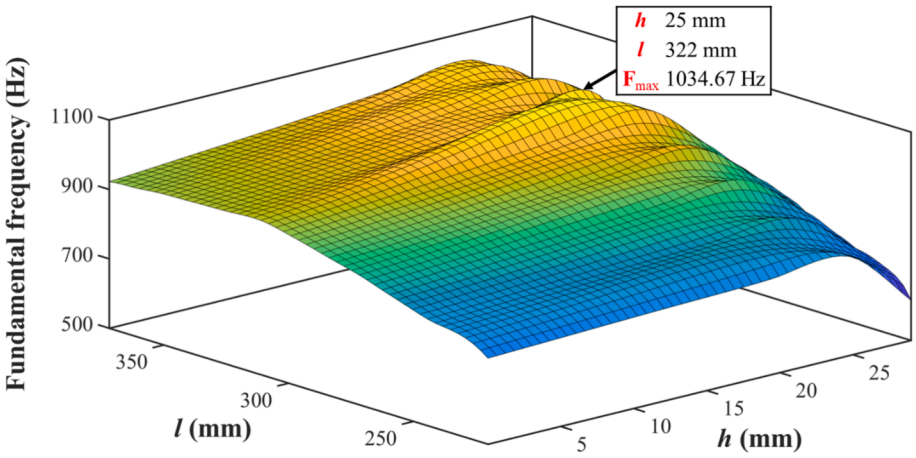

Fig. 6. Impact of l and h variations on fundamental frequency.

Table 2
Optimization results.

Parameter	Value
L	500 mm
l	310 mm
H	40 mm
h	24.4 mm

theoretically allowing measurements to proceed without further calibration. However, during the practical testing, we found this assumption to be unreliable. With varying input amplitudes, the output from the measurement platform exhibited significant nonlinear behavior, particularly under shock excitation. Therefore, if high measurement accuracy is required, additional calibration of the measurement platform is essential. To address this need, we proposed a transfer learning DNN calibration scheme.

3.1. Network design

In the calibration process, a transformation exists between the applied excitations and the actual responses, represented by Eq. (2). Here, **M** can be treated as a 6×15 transfer matrix that adjusts the 15 sensor channel responses into a six-dimensional generalized force. Calibration of the platform is usually done by determining matrix **M** via the generalized inverse matrix method. However, this approach models the entire system as linear, which cannot capture the inherent nonlinear behavior, ultimately limiting measurement accuracy. To improve this, we sought an alternative to **M** in Eq. (2) by employing a nonlinear transformation to more accurately represent the relationship between the actual response and the calibrated response. For this purpose, we developed a DNN-based calibration model.

$$\begin{bmatrix} Fx(\omega) \\ Fy(\omega) \\ Fz(\omega) \\ Mx(\omega) \\ My(\omega) \\ Mz(\omega) \end{bmatrix}_{\text{exc}} = \boldsymbol{M}(\omega)_{6\times 15} \begin{bmatrix} F_{x1}(\omega) \\ F_{yi}(\omega) \\ F_{z1}(\omega) \\ F_{x2}(\omega) \\ \vdots \\ F_{z5}(\omega) \end{bmatrix}_{\text{res}} \tag{2}$$

To retain the structural information in Eq. (1), the sensor outputs are first substituted into Eq. (1) for calculation, yielding uncalibrated six-dimensional measurement results. These measurements are then combined with the excitation values and subjected to a Fourier transform to obtain frequency-domain data $[F_{\text{res}}(\omega), F_{\text{exc}}(\omega)]$. For each frequency ω,

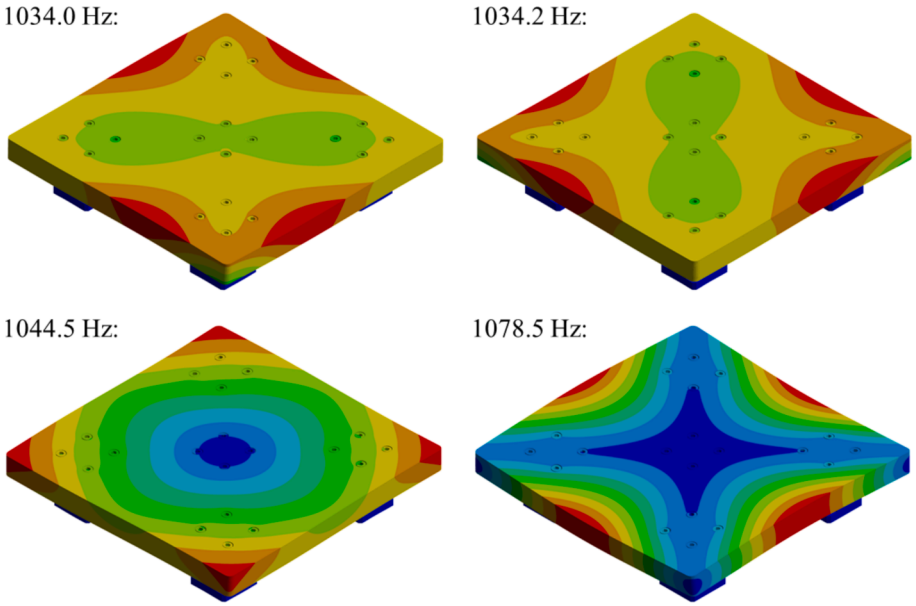

Fig. 7. First 4 modes of the upper plate optimization model.

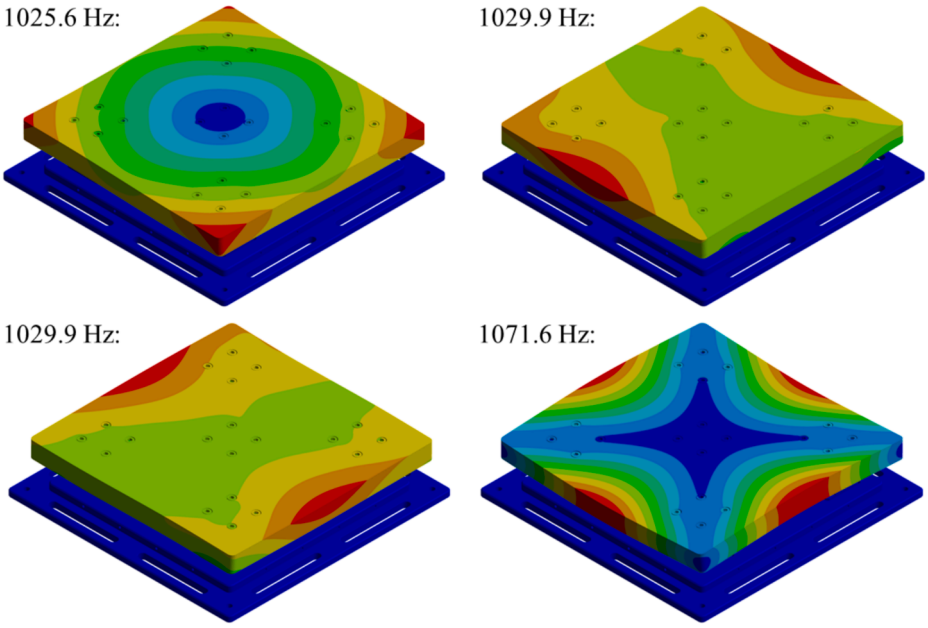

Fig. 8. First 4 modes of the overall structure.

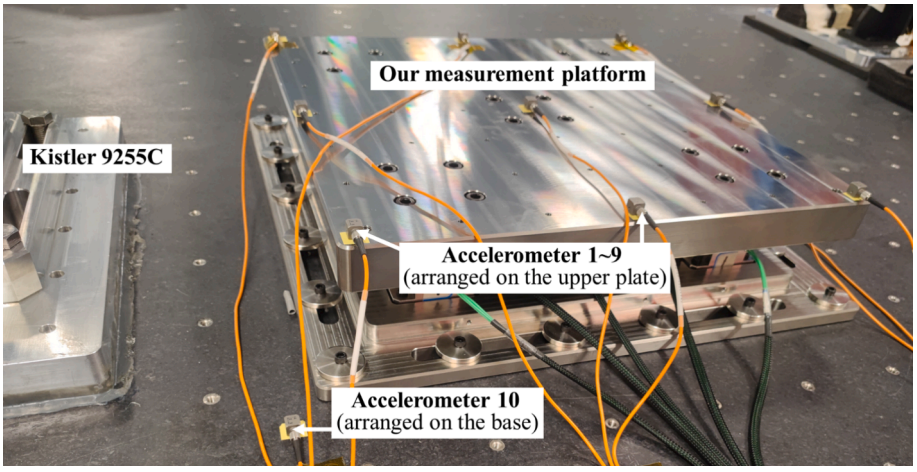

Fig. 9. Modal test setup for measurement platform.

the calibration process involves finding a DNN that converts the uncalibrated results $F_{\text{res}}(\omega)$ to the correct values $F_{\text{exc}}(\omega)$.

Since calibration is performed in the frequency domain, we observe that, unlike traditional neural network training problems, it is necessary to retain network parameters for each frequency point ω. Our research objective, therefore, is not merely to design a neural network with a highly complex structure to achieve ultimate fitting accuracy. Instead, a more important goal is to develop numerous network groups that are easy to train, exhibit good convergence properties, and provide high-precision fitting results. To achieve this, we initially trained the first DNN ($\omega = \omega_{\text{min}}$) using randomly initialized parameters and then used the trained DNN parameters at frequency ω as the starting input for training at frequency $\omega + \Delta\omega$. This transfer learning strategy significantly accelerates the training process for the following DNNs. Moreover, the use of transfer learning requires manual adjustment of only the detailed parameters in the first network, thereby further reducing the overall workload of the training process.

The structure of our designed DNN is illustrated in Fig. 11, the hidden layer comprises six fully connected (FC) layers. The configuration of the first five FC layers is identical: each FC layer generates 16 outputs, uses batch normalization, and applies the ReLU activation function. The sixth FC layer serves as the precursor to the output layer, generates 6 outputs and also utilizes the ReLU activation function, aligning with the non-negative nature of our objective function, which is compatible with the output range of the ReLU function. To compute the output at a given frequency ω, we used matrix $[F_{\text{res}}(\omega - \Delta\omega), F_{\text{res}}(\omega), F_{\text{res}}(\omega + \Delta\omega)]$ as the input instead of matrix $F_{\text{res}}(\omega)$. This choice is based on two primary considerations. First, the structure of measurement platform shows similarity across closely spaced frequency points, and leveraging response data from adjacent frequencies enhances system robustness and helps prevent overfitting. Second, ensuring an appropriate overlap between inputs at adjacent frequencies supports the implementation of transfer learning, which will be elaborated upon in subsequent chapters.

3.2. Training process

After establishing the calibration methodology, an excitation device capable of providing measurable six-dimensional generalized forces is required. We used an I-shaped tooling, as depicted in Fig. 12(a), to input these excitations. This method, as proposed in Ref. [28], uses a force

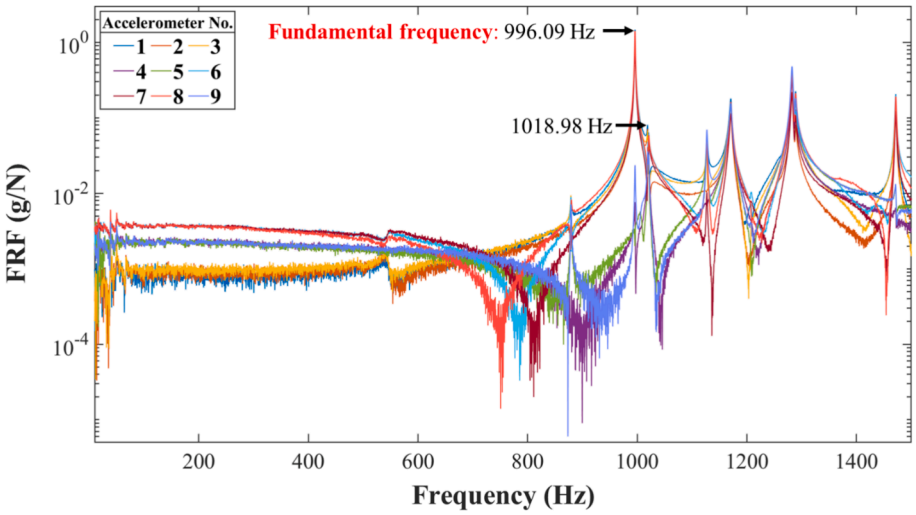

Fig. 10. Transfer function of the measurement platform.

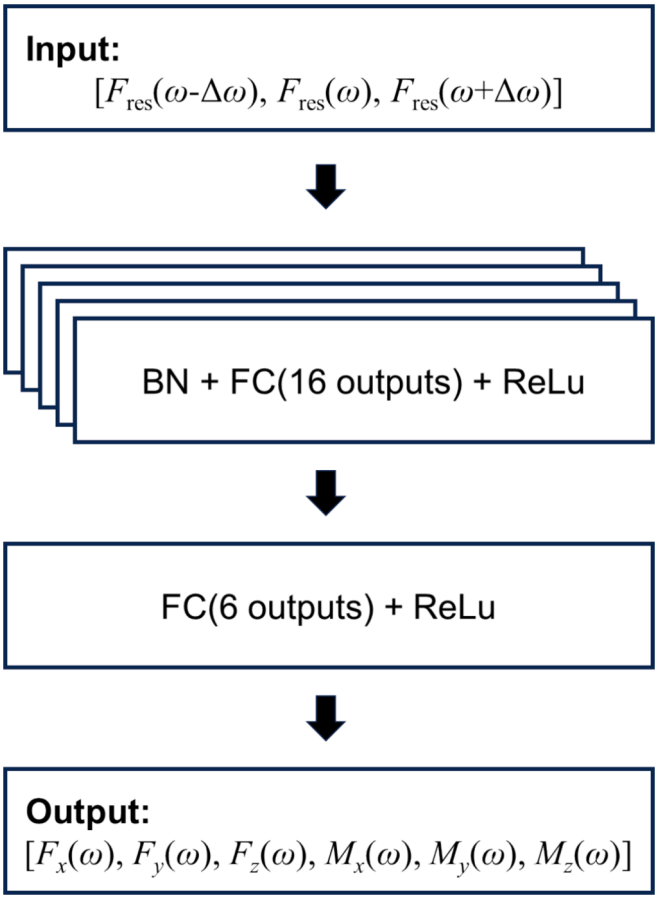

Fig. 11. Structure of the DNN.

hammer to apply impacts at different points on the tooling, generating force and moment inputs across various directions and magnitudes. By attaching accelerometers to the tooling, as shown in Fig. 12(b), the fundamental frequency was measured to be 3859.86 Hz, as displayed in Fig. 12(c). This frequency is over three times the fundamental frequency of our measurement platform, allowing the tooling to be considered as a rigid body when mounted on the platform's upper plate. Under these conditions, and to simplify calculations, the excitation applied to the tooling was transformed to the equivalent excitation at the center of the upper plate surface. Thus, the standard excitation values, i.e., the left side of Eq. (2), can be obtained.

For data collection, we selected 10 points on the surface of the tooling as input points for excitation. The dimension of each excitation was set normal to the surface, with each point impacted 40 times at varying force magnitudes, resulting in 400 data sets. These data will be used to train the neural network in the subsequent section. Fig. 13 illustrates the data collection process and the setup used.

The transfer learning training process is described as follows, with a detailed flowchart in Fig. 14 illustrating the operational steps of network training:

1. Preprocess the collected data, determine the frequency bandwidth for calibration, and divide the data according to different frequencies ω. There are 400 groups of data, each with $[F_{res}(\omega-\Delta\omega), F_{res}(\omega), F_{res}(\omega+\Delta\omega)]$ and the corresponding $F_{exc}(\omega)$.
2. Starting with $\omega=\omega_{min}$, initialize the weights and biases of each neuron using the He initialization method. Divide the 400 data sets into a training set and validation set with an 8:2 ratio.
3. Randomly divide the training set into mini-batches of size 16.
4. Use one mini-batch to compute the network output. The output of each neuron is calculated by Eq. (3), where the subscript (j, k) represents the k^{th} neuron in the k^{th} layer, and the function f denotes the ReLU activation function. The output of the final FC layer is the fitted result, as expressed in Eq. (4).

$$u_{(j,k)} = f\left[\sum_{i=1}^{16}(w_{(i,k)} \times u_{(j-1,i)} + b_{(i,k)})\right] \tag{3}$$

$$\boldsymbol{M}_{out} = [Fx, Fy, Fz, Mx, My, Mz]_{out} \tag{4}$$

5. Substitute $\boldsymbol{M}_{out}$ and $F_{exc}(\omega)$ into Eqs. (5) and (6) to calculate the root mean square error (RMSE) and loss. Apply the backpropagation algorithm to update the weights and biases of each neuron. For the initial case $\omega=\omega_{min}$, $Epoch_{max}$ is set to 300, as training the DNN from a random initial state requires more epochs to achieve convergence. For subsequent cases $\omega > \omega_{min}$, $Epoch_{max}$ is set to 100, as transfer learning enables faster convergence with fewer epochs.

$$RMSE = \frac{1}{6}\sqrt{\sum_{i=1}^{3}(F_i - F_{exc})^2 + \sum_{i=1}^{3}(M_i - M_{exc})^2} \tag{5}$$

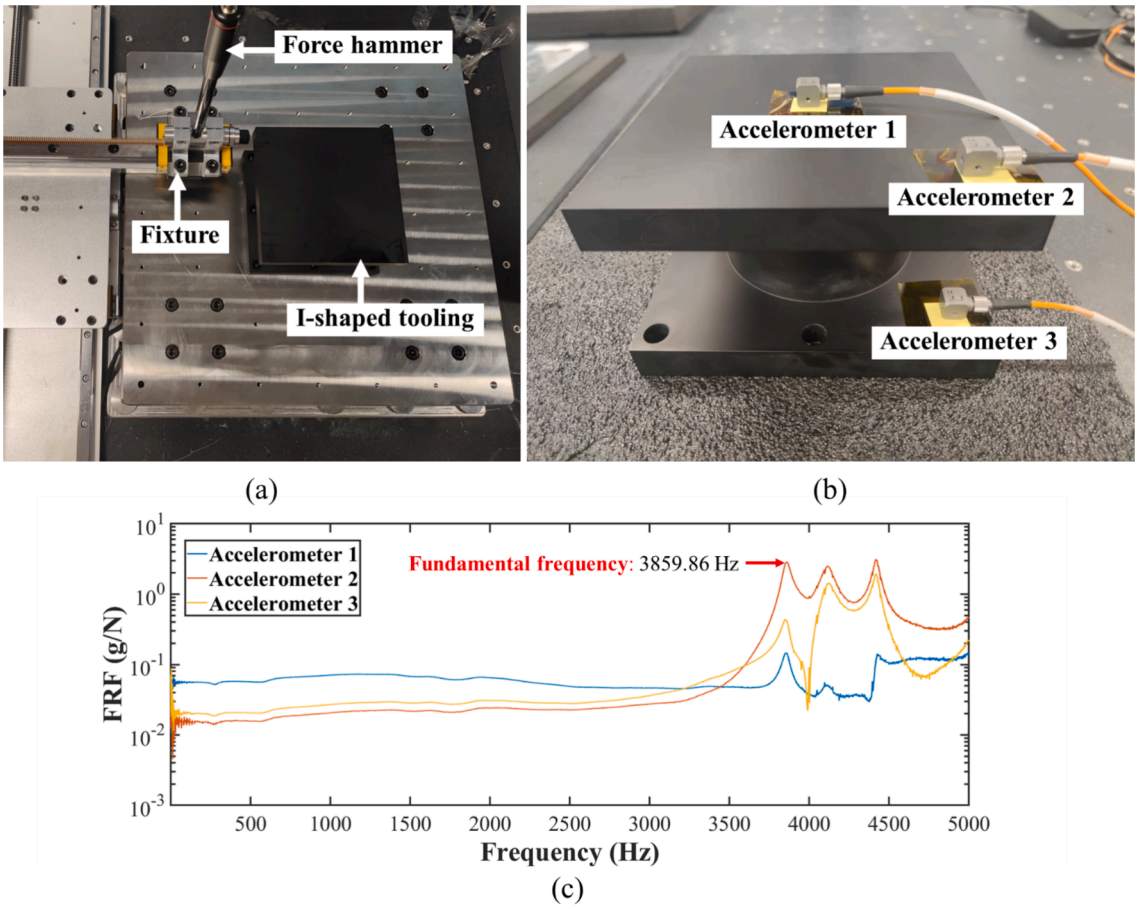

Fig. 12. I-shaped tooling, (a) Working condition; (b) Modal test preparation; (c) Modal test results.

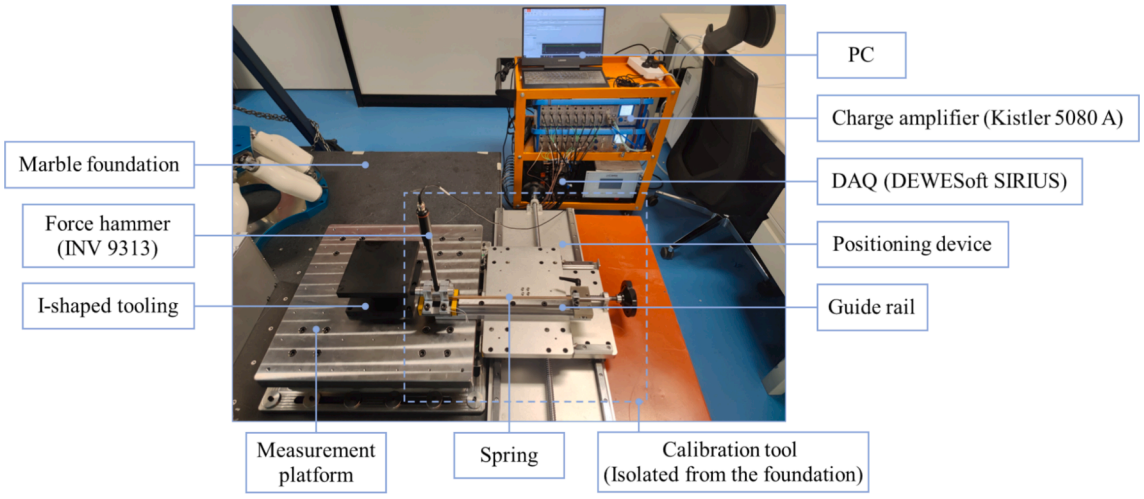

Fig. 13. Data collection site.

$$Loss = \frac{1}{6}\left[\sum_{i=1}^{3}(F_i - F_{exc})^2 + \sum_{i=1}^{3}(M_i - M_{exc})^2\right] \tag{6}$$

6. The learning rate is defined by Eq. (7), where Lr_0 denotes the initial learning rate, and $Epoch$ and $Epoch_{max}$ represent the current and maximum number of epochs, respectively. Eq. (7) ensures that a larger learning rate is used during the initial stages of training, allowing the network to converge more quickly. In later stages, a smaller learning rate is applied to refine the network and reach an optimal solution. Additionally, due to the retraining mechanism in subsequent training steps for underperforming networks, this adaptive learning rate also provides a cyclical learning rate training scheme to enhances their performance.

$$Lr = \frac{Lr_0}{2} \times \left(-\tanh\left(\frac{2\pi}{Epoch} \times \left(Epoch - \frac{Epoch_{max}}{2}\right)\right) + 1\right) \tag{7}$$

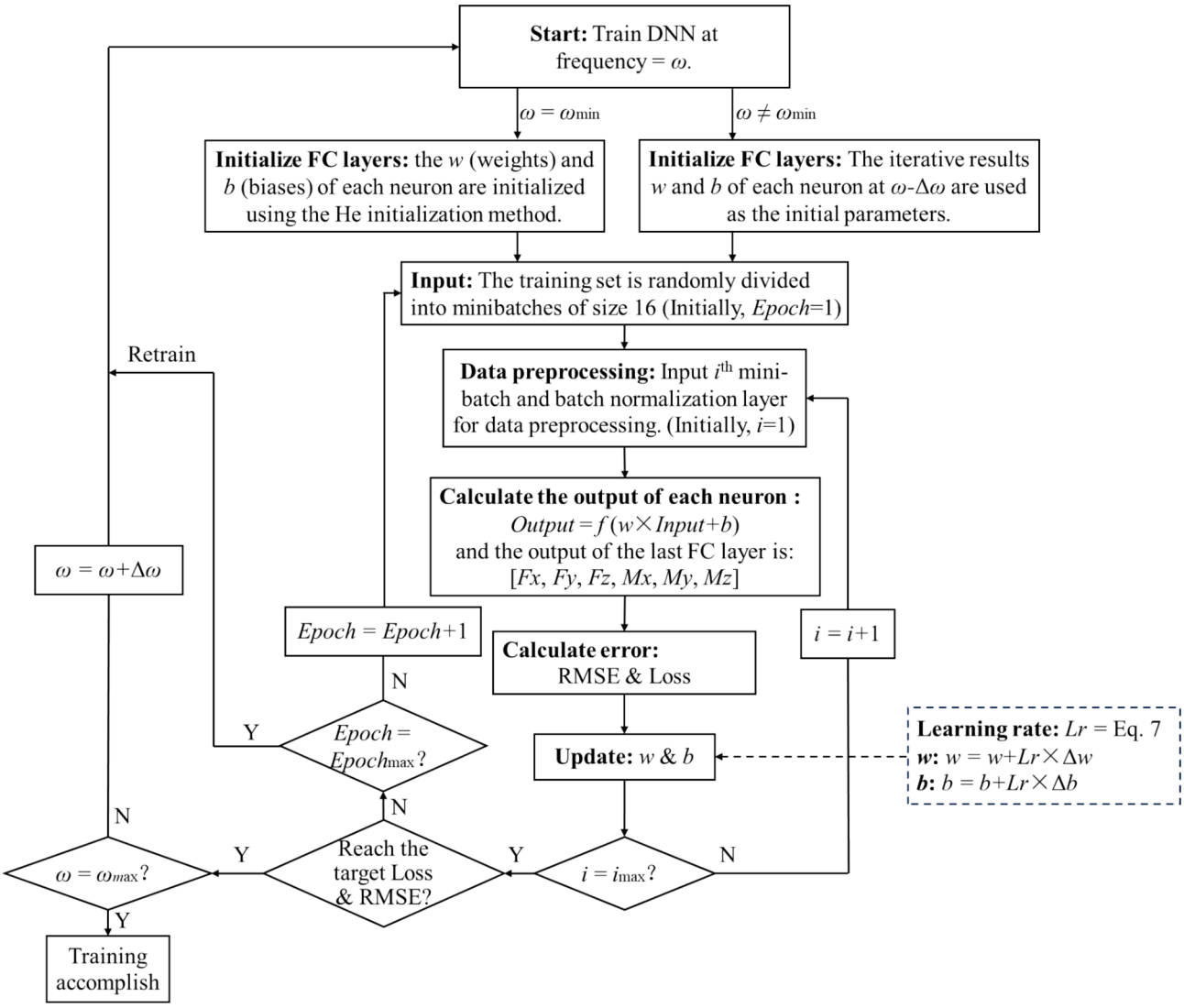

Fig. 14. Training process of the transfer learning DNN.

7. Repeat steps 4 and 5 with the next mini-batch. Once all mini-batches have been used, proceed to the next epoch and return to step 3, iterating until the target training and validation loss are reached or the maximum epoch limit is met.
8. After training completes, use the network to predict the six-dimensional generalized forces on the training and validation data sets. If the maximum and mean RMSE values meet the specified targets, the DNN training is considered complete; otherwise, retraining is required.
9. $\omega_{i+1} = \omega_i + \Delta\omega$, use the DNN parameters of ω_i as the initial parameters of ω_{i+1}, return to step 3 and perform transfer learning until $\omega = \omega_{max}$.

Using the above training scheme, we calibrated the measurement platform within the frequency band of 10 ~ 600 Hz; thus,ω_{min} and ω_{max} are set to 10 Hz and 600 Hz, respectively, with a $\Delta\omega$ of 0.4 Hz. In total, we trained 1476 neural networks, and the network structure and training method we designed performed effectively for this task.

Fig. 15 presents the RMSE on the training and validation sets for each frequency ω. Since the training set and validation set contain 320 and 80 data groups, respectively, the corresponding RMSE values are calculated 320 and 80 times. Therefore, we use the maximum and mean RMSE values to evaluate training performance. The results indicate that, across the entire frequency band, the maximum RMSE remains below 0.09 and the mean RMSE is below 0.02, demonstrating that the trained networks provide accurate fitting results. Additionally, although the RMSE values fluctuate, the RMSEs of the training and validation sets remain closely aligned, which confirms that our network structure is robust and does not exhibit overfitting.

Additionally, as shown in Fig. 16, we analyzed the output variation in response to changes in input across six dimensions and calculated the relative errors, as summarized in Table 3. Across the entire dataset, the maximum relative error in the predictions for the dimensions *Fx*, *My*, and *Mz* is less than 4 %, while the maximum relative error for *Fz*, *Mx*, and *My* is less than 8 %. This discrepancy arises from the lower stability of our calibration tool in vertical excitation compared to horizontal excitation. Overall, these results demonstrate that the network performs well within the calibration range, with a strong fitting performance across varying input force amplitudes.

4. Testing and analysis of results

After the training process, we conducted detailed tests to evaluate their performance. During testing, excitations were applied to the measurement platform with the I-shaped tooling installed, enabling us to calculate the theoretical six-dimensional generalized force inputs.

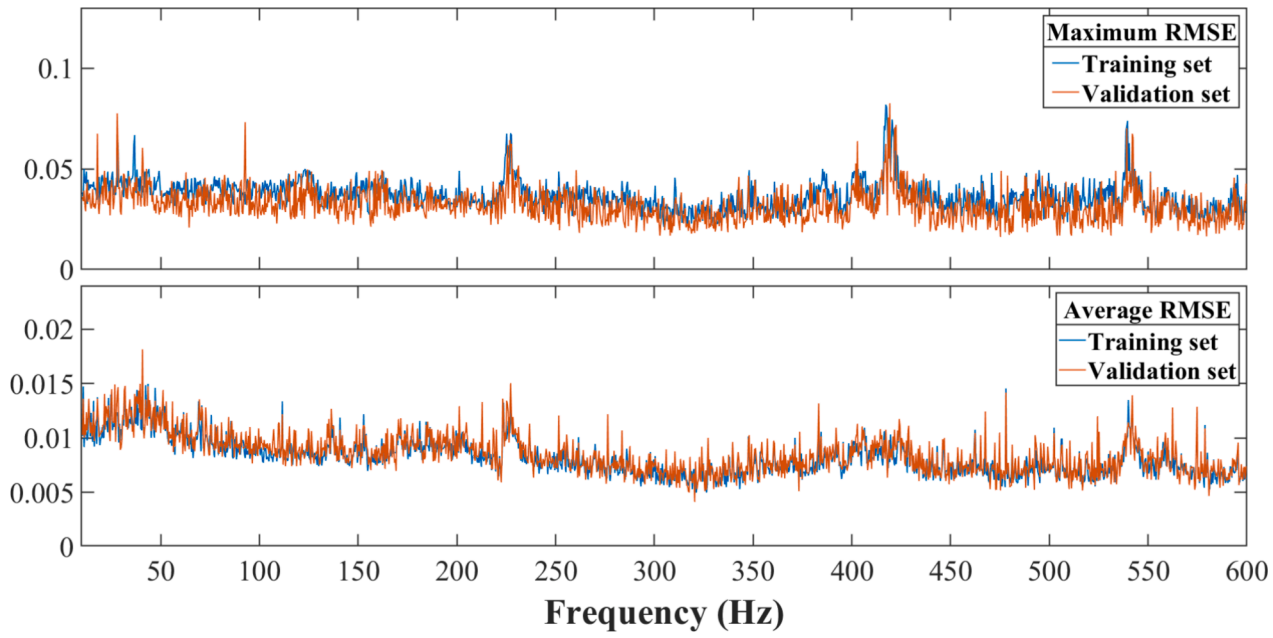

Fig. 15. RMSE of the networks.

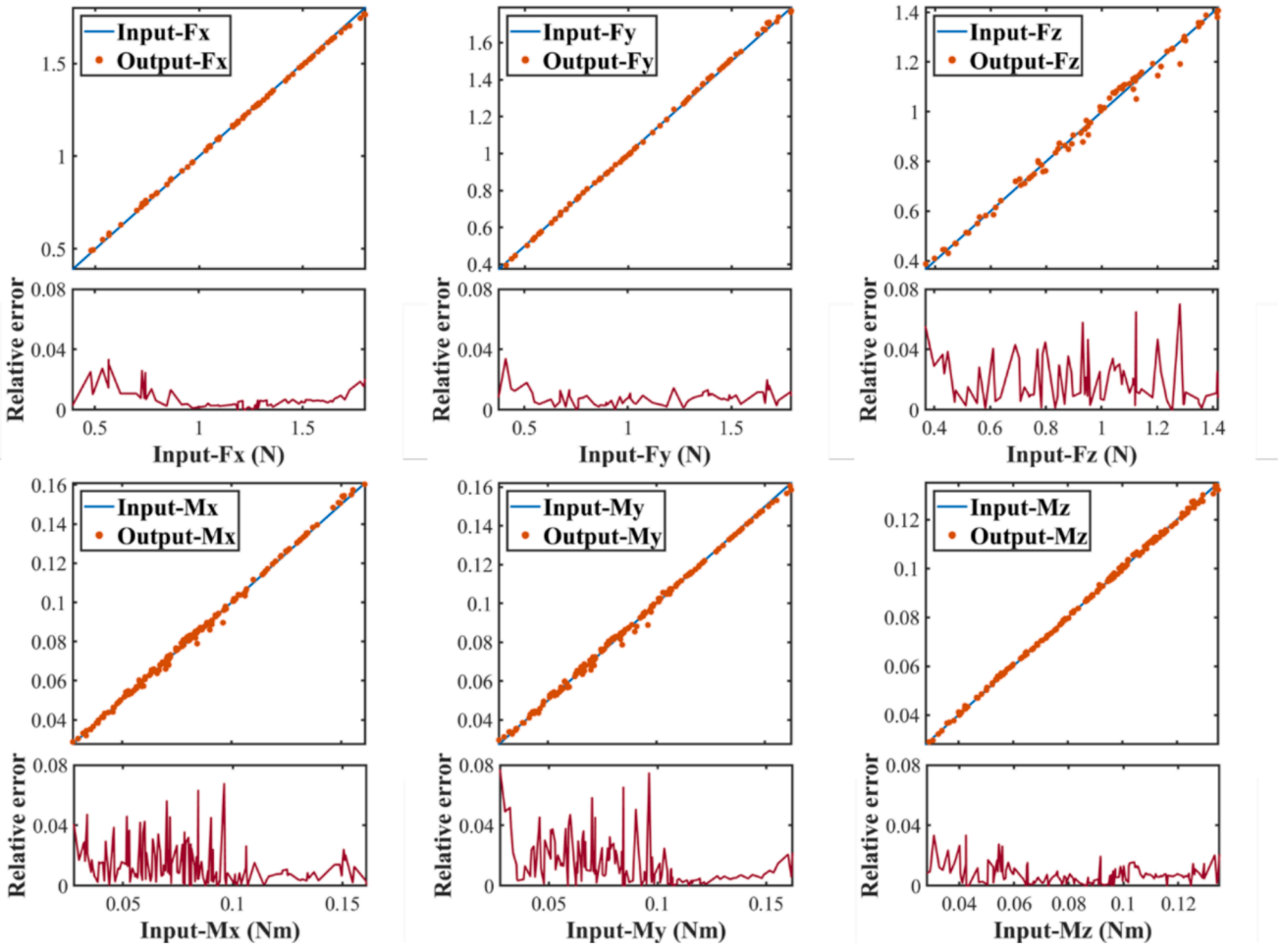

Fig. 16. Outputs and relative errors in six dimensions.

Table 3
Maximum relative errors in six dimensions.

Input force/moment	Maximum relative error
Fx	3.33 %
Fy	3.38 %
Fz	7.00 %
Mx	6.76 %
My	7.73 %
Mz	3.33 %

When excitation is applied in the *x* direction, the expected response should appear in *Fx*, *My*, and *Mz*, with no response in the remaining three dimensions. Similarly, when the excitation is in the *y* direction, responses are expected in *Fy*, *Mx*, and *Mz*, and for excitation in the *z* direction, responses should appear in *Fz*, *Mx*, and *My*. By applying excitation sequentially in the *x*, *y*, and *z* directions, we can verify the predicted results across all six directions.

4.1. Measurement without DNN calibration

Although the sensors used in our system are dynamically calibrated in factory, experimental results demonstrate that the measurement accuracy of the platform does not meet the exacting requirements without additional calibration. Fig. 17 provides an example where excitations are applied in the three dimensions *Fy*, *Mx*, and *Mz*, while the excitations in the remaining three dimensions are zero. Without calibration using the transfer learning DNN, the sensor outputs exhibit significant deviations from the actual inputs. Due to coupling effects between the sensors' output dimensions, non-zero signals are observed in directions where the outputs should theoretically be zero. Additionally, Fig. 17 also shows that, in certain frequency bands, small structural couplings between the measurement platform and the marble foundation result in responses exceeding those of the target measurement dimensions, further distorting the measured values.

4.2. Measurement with transfer learning DNN

The measurement results without neural network calibration are significantly impacted by coupling effects between the sensor output dimensions and the structural coupling between the measurement platform and the marble foundation. Our calibration method effectively addresses both issues. Fig. 18 presents the calibrated outputs for excitations in the *x*, *y*, and *z* directions, respectively. The figure shows that, in the excitation direction, the outputs align closely with the inputs, while in non-excitation directions, the outputs are nearly zero, demonstrating that our neural network calibration successfully addresses both the fitting and decoupling challenges. As shown in Table 4, the average relative error of the response data across all six dimensions remains below 3 % throughout the entire frequency band, indicating that our measurement system reliably performs within the calibrated frequency range. In contrast, calibrating only the sensors without further calibrating the platform leads to relative measurement errors exceeding 25 % across all six dimensions, rendering precise measurements infeasible.

5. Conclusions

This paper presents a comprehensive discussion of the design, analysis, calibration, and testing of a six-dimensional micro-vibration measurement platform. To perform micro-vibration tests for large space payloads, a larger six-dimensional generalized force plate is required. In response to this demand, we designed and constructed a measurement platform with a 5-sensor configuration. Compared to the traditional 4-sensor force plate, an additional sensor positioned at the center of the platform enhances the fundamental frequency of the structure. Through finite element analysis, we determined that the fundamental frequency of the platform in the 5-sensor configuration is increased by 12 % relative to the 4-sensor configuration, significantly optimizing the structural parameters of the measurement platform. Additionally, by optimizing certain parameters of the upper plate with the fundamental frequency as the design target, we further improved the structure's fundamental frequency. The final platform has a fundamental frequency of 996 Hz, closely matching our FEA result of 1034 Hz, which meets the measurement requirements.

Following the structural design, we further studied the calibration method. In previous engineering projects, it was commonly assumed that a force plate with multiple calibrated sensors did not require further calibration. However, we found that due to nonlinear effects, high-precision measurements could not be achieved without dynamic calibration using a model capable of nonlinear fitting. To address this, we proposed a novel transfer learning DNN model to calibrate the platform. At each pair of adjacent frequencies, the trained parameters of the preceding network serve as initialization parameters for the subsequent network, thereby implementing transfer learning. For network training, transfer learning implies that, once the DNN hyperparameters at $\omega_{\min}$ are adjusted, high-performance networks can be obtained across all frequency points within the entire frequency band. At a deeper level, the transfer learning process reflects the continuity of the structural physical properties within a contiguous frequency band. With the transfer learning DNN model, we successfully reduced the measurement error to less than 5 % and met the requirements for high-precision measurement.

Although the measurement platform in this paper is designed for micro-vibration testing of satellite payloads, its large upper plate, excellent rigidity, and high measurement accuracy make it suitable for more general vibration testing of large motion mechanisms. However,

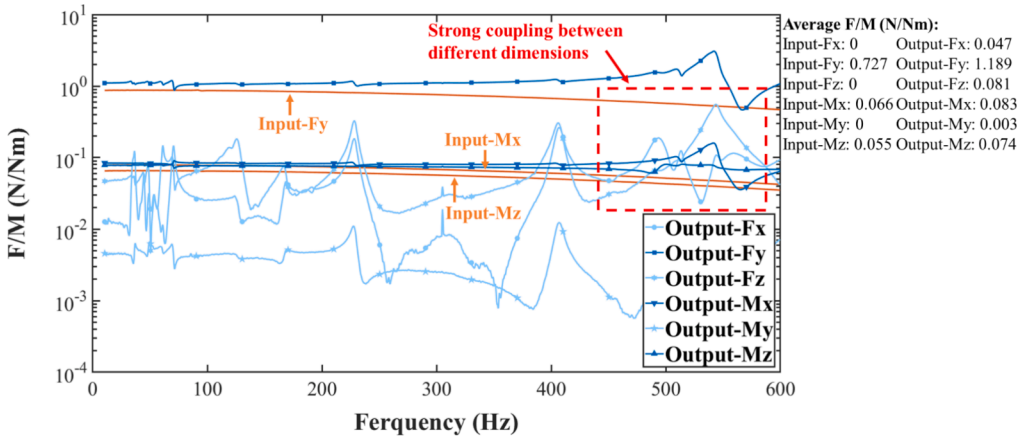

Fig. 17. Measurements without transfer learning DNN calibration.

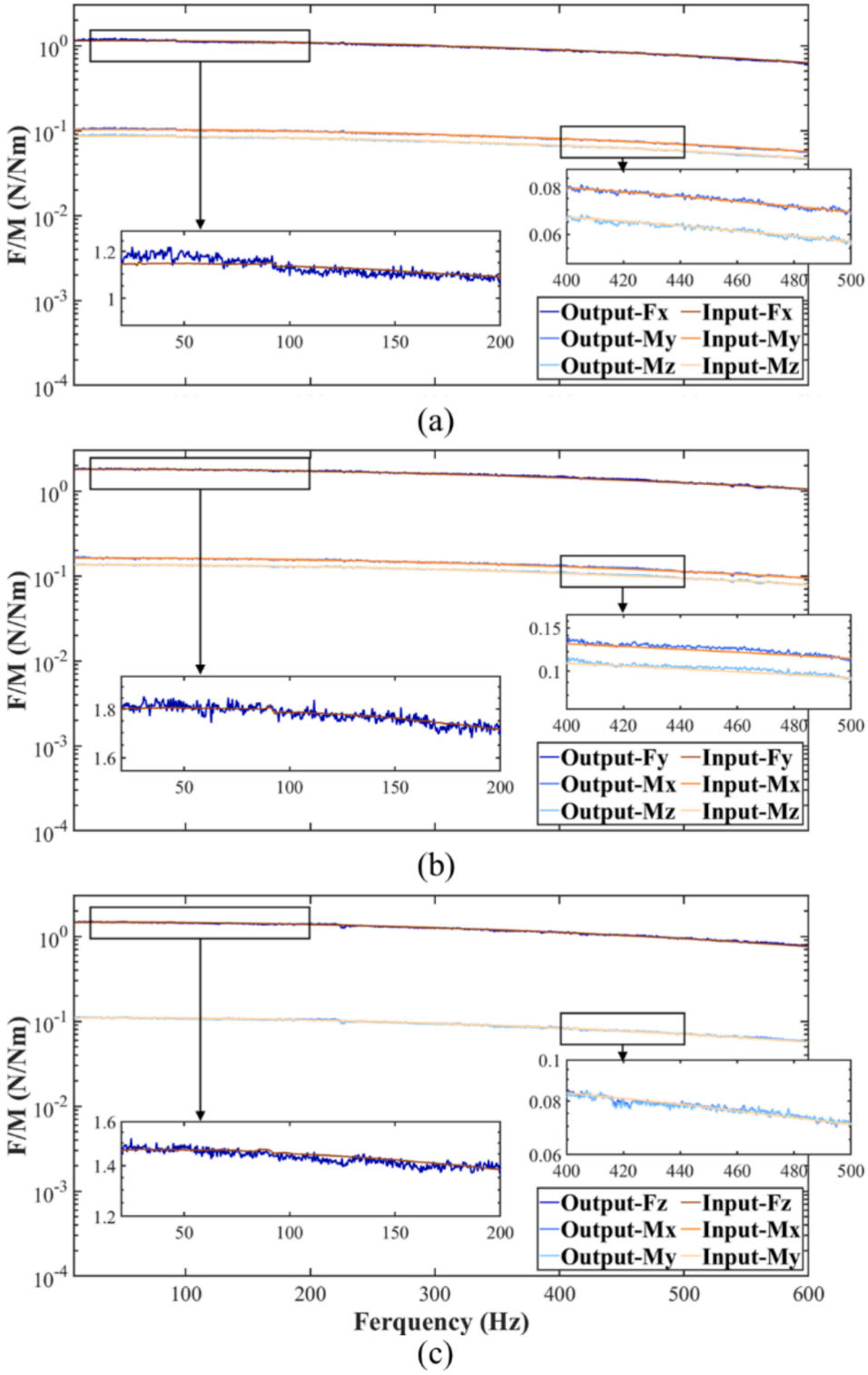

Fig. 18. Comparison between measured and theoretical magnitudes: (a)*Fx*, *My*, *Mz*; (b)*Fy*, *Mx*, *Mz*; (c)*Fz*, *Mx*, *My*.

Table 4
Test results in six dimensions.

Input force/moment	Average relative errors
Fx	2.38 %
Fy	1.39 %
Fz	2.80 %
Mx	2.18 %
My	2.65 %
Mz	1.90 %

compared to vibration sources on satellites, general vibration sources may have larger vibration amplitudes, and their design may not prioritize optimization in terms of volume and mass to the same extent. Therefore, in extending its application, more attention must be paid to collecting appropriate calibration data that covers the relevant amplitudes and frequency bands. Additionally, when the vibration source is relatively heavy, further structural testing may be required to avoid potential structural coupling.

CRediT authorship contribution statement

Haodong Cui: Writing – original draft, Visualization, Validation, Software, Methodology, Investigation, Formal analysis, Data curation. **Mingming Xu:** Writing – review & editing, Supervision, Resources, Funding acquisition, Conceptualization. **Jiangpei Dou:** Resources, Project administration, Funding acquisition.

Declaration of competing interest

The authors declare that they have no known competing financial interests or personal relationships that could have appeared to influence the work reported in this paper.

Acknowledgments

This work was supported by the National Natural Science Foundation of China (No. U2031210).

Data availability

Data will be made available on request.

References

[1] C. Wu, K. Guo, J. Sun, et al., Active vibration control in robotic grinding using six-axis acceleration feedback, Mech. Syst. Sig. Process. 214 (2024) 111379, https://doi.org/10.1016/j.ymssp.2024.111379.
[2] J. Wu, X. Tang, F. Peng, et al., A novel mode coupling mechanism for predicting low-frequency chatter in robotic milling by providing a vibration feedback perspective, Mech. Syst. Sig. Process. 216 (2024) 111424, https://doi.org/10.1016/j.ymssp.2024.111424.
[3] B. Li, C. Su, W. Zhao, et al., A novel method of suppressing machining vibration in robotic milling using magneto-rheological foam damper, Chin. J. Aeronaut. 37 (2024) 522–543, https://doi.org/10.1016/j.cja.2024.04.012.
[4] M. Newman, M. Khoshdarregi, Automatic Structural Identification and Vibration Suppression of Industrial Robots using a Custom Active Damper. 22nd International Conference on Control, Automation and Systems, (2022). https://doi.org/10.23919/ICCAS55662.2022.10003880.
[5] C. Sancak, M. Itik, Out-of-plane vibration suppression and position control of a planar cable-driven robot, IEEE-ASME Trans. Mechatron. 27 (2022) 1311–1320, https://doi.org/10.1109/TMECH.2021.3089588.
[6] H. Habbouche, Y. Amirat, T. Benkedjouh, et al., Digital twin-based gearbox fault diagnosis using variational mode decomposition and dynamic vibration modeling, Measurement 246 (2025) 116669, https://doi.org/10.1016/j.measurement.2025.116669.
[7] Y. Guan, Z. Meng, F. Gu, et al., Fault diagnosis of wind turbine structures with a triaxial vibration dual-branch feature fusion network, Reliab. Eng. Syst. Saf. 256 (2025) 110746, https://doi.org/10.1016/j.ress.2024.110746.
[8] D. Su, X. Cui, Two suggested configurations for the Chinese space telescope, Res. Astron. Astrophys. 14 (2014) 1055–1060, https://doi.org/10.1088/1674-4527/14/9/001.
[9] Y. Gong, X. Liu, Y. Cao, et al., Cosmology from the Chinese Space Station Optical Survey (CSS-OS), Astrophys J 883 (2019) 203, https://doi.org/10.3847/1538-4357/ab391e.
[10] M. Xia, Z. Xu, K. Han, et al., Dynamic disturbance force measurement platform for large moving device in spacecraft, J. Sound Vib. 447 (2019) 61–77, https://doi.org/10.1016/j.jsv.2019.01.053.
[11] J. Luo, L. Chen, H. Duan, et al., TianQin: a space-borne gravitational wave detector, Classical Quant. Grav. 33 (2016) 035010, https://doi.org/10.1088/0264-9381/33/3/035010.
[12] K. Danzmann, et al., Section 5 System requirements & spacecraft key factors, Laser interferometer space antenna, (2017).
[13] S. Kwon, Y. Jeon, H. Oh, Micro-jitter attenuation of spaceborne cooler by using a blade-type hyperelastic shape memory alloy passive isolator, Cryogenics 87 (2017) 35–48, https://doi.org/10.1016/j.cryogenics.2017.08.011.
[14] H. Luo, C. Fan, Y. Li, et al., Design and experiment of micro-vibration isolation system for optical satellite, Eur. J. Mech. A Solids 97 (2023) 104833, https://doi.org/10.1016/j.euromechsol.2022.104833.
[15] H. Oh, K. Lee, M. Jo, A passive launch and on-orbit vibration isolation system for the spaceborne cryocooler, Aerosp. Sci. Technol. 28 (2013) 324–331, https://doi.org/10.1016/j.ast.2012.11.013.
[16] H. Alkomy, J. Shan, Modeling and validation of reaction wheel micro-vibrations considering imbalances and bearing disturbances, J. Sound Vib. 492 (2021) 115766, https://doi.org/10.1016/j.jsv.2020.115766.
[17] D. Addari, G.S. Aglietti, M. Remedia, Experimental and numerical investigation of coupled microvibration dynamics for satellite reaction wheels, J. Sound Vib. 386 (2017) 225–241, https://doi.org/10.1016/j.jsv.2016.10.003.
[18] M.M. Longato, T. Hughes, V. Yotov, et al., Microvibration simulation of reaction wheel ball bearings, J. Sound Vib. 567 (2023) 117909, https://doi.org/10.1016/j.jsv.2023.117909.
[19] C. Kang, Closed-form force sensing of a 6-axis force transducer based on the Stewart platform, Sens. Actuator A Phys. 90 (2001) 31–37.
[20] Y. Zhao, T. Zhao, R. Wen, et al., Performance analysis and optimization of sizable 6-axis force sensor based on Stewart platform. In: IEEE International Conference on Mechatronics and Automation, (2007).
[21] Z. Jia, S. Lin, W. Liu, Measurement method of six-axis load sharing based on the Stewart platform, Measurement 43 (2010) 329–335, https://doi.org/10.1016/j.measurement.2009.11.005.
[22] T. Jang, B. Lim, M. Kim, The canonical Stewart platform as a six DOF pose sensor for automotive applications, J. Mech. Sci. Technol. 32 (2018) 5553–5561, https://doi.org/10.1007/s12206-018-1101-0.
[23] S. Zhou, J. Sun, W. Chen, et al., Method of designing a six-axis force sensor for stiffness decoupling based on Stewart platform, Measurement 148 (2019) 106966, https://doi.org/10.1016/j.measurement.2019.106966.
[24] Y. Li, G. Wang, J. Zhang, et al., Dynamic characteristics of piezoelectric six-dimensional heavy force/moment sensor for large-load robotic manipulator, Measurement 45 (2012) 1114–1125, https://doi.org/10.1016/j.measurement.2012.01.028.
[25] C. Zhou, M. Xia, Z. Xu, Design and optimization of a quadrupedal dynamic disturbance force measurement platform using strain gauges, Mech. Syst. Sig. Process. 188 (2023) 110032, https://doi.org/10.1016/j.ymssp.2022.110032.
[26] C. Zhou, M. Xia, Z. Xu, A piezoelectric load-sharing-based platform for measuring dynamic six-dimensional forces/moments of large equipment in spacecraft, Precis. Eng. 83 (2023) 112–123, https://doi.org/10.1016/j.precisioneng.2023.05.009.
[27] C. Zhou, M. Xia, Z. Xu, Fault-tolerant dynamic force/moment measuring platform for large spacecraft equipment using the GAALBP fusion algorithm, Mech. Syst. Sig. Process. 211 (2024) 111185, https://doi.org/10.1016/j.ymssp.2024.111185.
[28] M. Xia, C. Zhou, E. Zhang, et al., A dynamic disturbance force measurement system based on array sensor for large moving device in spacecrafts, J. Sound Vib. 535 (2022) 117069, https://doi.org/10.1016/j.jsv.2022.117069.
[29] https://kistler.cdn.celum.cloud/SAPCommerce_Download_original/003-051e.pdf.
[30] https://kistler.cdn.celum.cloud/SAPCommerce_Download_original/003-460e.pdf.
[31] S. Liu, H. Tzo, A novel six-component force sensor of good measurement isotropy and sensitivities, Sens. Actuator A Phys. 100 (2002) 223–230.
[32] R. Ranganath, P.S. Nair, T.S. Mruthyunjaya, et al., A force-torque sensor based on a Stewart Platform in a near-singular configuration, Mech. Mach. Theory 39 (2004) 971–998, https://doi.org/10.1016/j.mechmachtheory.2004.04.005.
[33] Y. Li, G. Wang, X. Yang, et al., Research on static decoupling algorithm for piezoelectric six axis force/torque sensor based on LSSVR fusion algorithm, Mech. Syst. Sig. Process. 110 (2018) 509–520, https://doi.org/10.1016/j.ymssp.2018.03.015.
[34] Q. Liang, J. Long, C. Gianmarc, Novel decoupling algorithm based on parallel voltage extreme learning machine (PV-ELM) for six-axis F/M sensors, Rob. Comput. Integr. Manuf. 57 (2019) 303–314, https://doi.org/10.1016/j.rcim.2018.12.014.
[35] T. Li, H. Zheng, A. Pan, et al., BP method with rectified linear unit-based nonlinear decoupling for 3-Axis FBG force sensor, IEEE Sens. J. 21 (2021) 2972–2979, https://doi.org/10.1109/JSEN.2020.3022663.
[36] H. Oh, U. Kim, G. Kang, et al., Multi-axial force/torque sensor calibration method based on deep-learning, IEEE Sens. J. 18 (2018) 5485–5496, https://doi.org/10.1109/JSEN.2018.2834727.
[37] C. Zhou, M. Xia, C. Li, et al., Structural optimization and dynamic calibration for load sharing dynamic force measurement platform based on MIGA and SVR, Measurement 218 (2023) 113139, https://doi.org/10.1016/j.measurement.2023.113139.